JOM, Vol. 75, No. 11, 2023
https://doi.org/10.1007/s11837-023-05973-6




# Synthesis and Sintering of Ultrafine $MoSi_2$-$WSi_2$ Composite Powders

HE-QIANG CHANG[1] and GUO-HUA ZHANG[1,2]

1.—State Key Laboratory of Advanced Metallurgy, University of Science and Technology Beijing, Beijing 100083, China. 2.—e-mail: ghzhang0914@ustb.edu.cn

In this work, ultrafine $MoSi_2$-$WSi_2$ composite powders with different volume fractions of $WSi_2$ were controllably prepared via silicothermic reduction of $MoS_2$-$WS_2$ mixtures. The micromorphology observation shows that the as-prepared particles inherited the sheet-like morphology of $MoS_2$ or $WS_2$ and consisted of ultrafine grains. The vacuum pressureless sintering results indicated that the addition of $WSi_2$ can greatly enhance the mechanical properties of the $MoSi_2$ matrix, attributed to the solid solution strength of $WSi_2$, grain refinement and increase of relative density of the samples caused by the introduction of Fe element. When the volume fraction of $WSi_2$ was between 1% and 20%, after sintering at 1500°C for 2 h, the $MoSi_2$-20 vol.% $WSi_2$ composite sample had the highest densification degree, hardness, and flexural strength of 95.21%, 10.72 GPa and 297 MPa, respectively. The $MoSi_2$-10 vol.% $WSi_2$ composite sample had a maximum fracture toughness value of 7.28 MPa $m^{1/2}$.

## INTRODUCTION

As a unique class of intermetallic compounds, refractory metal silicides (e.g., $MoSi_2$, $WSi_2$, $NbSi_2$ and $TaSi_2$) have special physicochemical characteristics, such as good electrical conductivity, ultra-high melting point, great oxidation resistance and excellent thermal stability, and have been widely utilized in the field of microelectronics and ceramics.[1–6] Among them, $MoSi_2$ has a high melting point of 2030°C, a medium density of 6.24 g/$m^3$, excellent elevated oxidation resistance (> 1600°C), relatively low thermal expansion coefficient (8.1 * $10^{-6}$ $K^{-1}$) and great thermal conductivity (25 W/m K).[4] As a result, $MoSi_2$ has received much attention in various application fields such as advanced aerospace, electric heating elements, high-temperature structural materials, microelectronic devices and electrocatalysts. However, the intrinsic limitations of low ductility (< 1000°C),[5] poor room temperature toughness and high temperature creep strength (> 1200°C), as well as "pesting" oxidation phenomenon between 400°C and 600°C greatly limit the application of $MoSi_2$.[6]

To overcome these intrinsic limitations, many researchers have focused on further improving the mechanical properties of $MoSi_2$ materials in terms of material design and fabrication techniques.[6–15] Among the material design strategies, reducing the grain size[7,8] and second-phase nanoparticle (hard ceramic phase) reinforcement have been proved to be effective avenues.[4,9] Timothy et al. demonstrated that reducing the grain size of $MoSi_2$ to the nanoscale can greatly enhance its mechanical properties, such as hardness, flexural strength and fracture toughness.[7] Additionally, many studies have shown that the addition of the hard ceramic phase nanoparticles such as $ZrO_2$,[10,11] SiC,[11,12] $Si_3N_4$,[13] $Al_2O_3$,[14] $Mo_5Si_3$,[15] etc., can enhance the mechanical properties of $MoSi_2$ matrix. Apart from the above methods, alloying with Al,[16,17] Re,[17] or W[18] is also considered a promising strategy. In particular, $WSi_2$ has the same crystal structure and nearly the same lattice parameters as $MoSi_2$,[19] enabling $WSi_2$ to form a solid solution with $MoSi_2$. A major improvement in mechanical properties has been realized by alloying $MoSi_2$ with $WSi_2$.[5,18–21]

(Received January 30, 2023; accepted June 19, 2023; published online July 11, 2023)

In recent years, many routes have been proposed for preparing $MoSi_2$-$WSi_2$ composite powder,[8,18,20–22] such as mechanical alloying (MA),[8,22] self-propagating high temperature synthesis (SHS)[18,21] and mechanically assisted self-propagating high temperature synthesis (MASHS).[20] MA is the most commonly reported method for preparing $MoSi_2$-$WSi_2$ composite powders, but impurities such as iron will be introduced during the ball milling process. SHS can prevent the induction of impurities and guarantee the purity of the product, but in most cases, coarse particles will be acquired.[20] The above methods all select pure Mo and W powder as raw materials. However, the production of Mo from $MoS_2$ requires a long and complicated process, resulting in high cost of Mo. Given these conditions, Zhang et al.[23–25] proposed a short, green and low-cost route to synthesize ultrafine $MoSi_2$ or $WSi_2$ powders through silicothermic reduction of $MoS_2$ or $WS_2$. Therefore, in this work, ultrafine $MoSi_2$-$WSi_2$ composite powders with different volume fractions of $WSi_2$ were synthesized via silicothermic reduction of $MoS_2$-$WS_2$ mixtures.

Due to their high melting point, pressure-assisted routes such as hot-pressing (HP) and spark plasma sintering (SPS) are commonly used to sinter refractory metal silicides.[4–6,9,10] However, pressure-assisted methods are difficult to use for the sintering of special-shaped samples.[26] Generally speaking, the prepared powder will adsorb gases such as $O_2$, $N_2$ and other gases, and the adsorbed gases will have a negative impact on the sintered product. According to the ideal gas law Eq. 1, where $p$, $V$, $n$, R and $T$ are the gas pressure (Pa), gas volume ($m^3$), gas molar amount (mol), molar gas constant (8.31 J/(mol K)) and temperature (K), respectively, a lower $p$ will lead to a lower $n$ during the sintering process of this work in the conditions of constant $T$ and $V$. Therefore, vacuum can reduce the interferences of $O_2$, $N_2$ and other gases on the sample, making the sample purer.[20,21] Therefore, vacuum pressureless sintering was used to sinter the ultrafine $MoSi_2$-$WSi_2$ composite powders, prepared through silicothermic reduction of $MoS_2$-$WS_2$ mixtures. Furthermore, the sintering behavior of ultrafine $MoSi_2$-$WSi_2$ composite powders and the mechanical properties of corresponding sintered samples were studied in detail.

$$pV = nRT \tag{1}$$

## MATERIALS AND METHODS

### Raw Materials

$MoS_2$ (98.5 wt.%), $WS_2$ (99 wt.%) and Si (99 wt.%) reagents were used as molybdenum, tungsten and silicon sources, respectively. Both $MoS_2$ and $WS_2$ powders have sheet-like structures with lateral dimensions of about 10 $\mu$m (see supplemental material Fig. S1a) and several $\mu$m (see supplemental material Fig. S1b), respectively, and the Si particles are composed of many Si nano grains (~300 nm, see supplemental material Fig. S1c). Additionally, CaO (99 wt.%) was utilized as desulfurizer. $MoS_2$, Si and CaO reagents were purchased from Sinopharm Chemical Reagent Co., Ltd., and $WS_2$ reagent was purchased from Shanghai Macklin Biochemical Co., Ltd.

### Preparation of $MoSi_2$-$WSi_2$ Composite Powders

Table I shows the raw material compositions for preparing 20 g $MoSi_2$-$WSi_2$ composite powders with 1 vol.%, 5 vol.%, 10 vol.% and 20 vol.% $WSi_2$. The schematic illustration of the preparation for the $MoSi_2$, $WSi_2$ and $MoSi_2$-$WSi_2$ composite powders are shown in Fig. 1. In a typical synthesis, approximately 5 g of the mixed raw material (according to Table I) was compressed into a cuboid, and seven cuboids were placed in an alumina crucible and wrapped with 20 g desulfurizer CaO. Next, the crucible containing the sample was placed into a quartz tube and reacted at 1100°C for 2 h in an Ar atmosphere. After the reaction was completed, the sample wrapped by desulfurization product layer can be obtained, and there is a clear boundary between the two; the target product was separated from the desulfurization product for further characterization and sintering.[23] For comparison, $MoSi_2$ and $WSi_2$ powders were also prepared at 1100°C. In addition, $MoSi_2$ powders were also prepared at 1000°C and 1200°C to research the effect of the grain size of $MoSi_2$ powders on the sintering behavior.

### Sintering of $MoSi_2$-$WSi_2$ Composite Powders

The prepared $MoSi_2$, $WSi_2$ and $MoSi_2$-$WSi_2$ composite powders were compressed into green compacts (each green compact weighted about 5 g) under a uniaxial pressure of 150 MPa with 2 wt.% paraffin as a binder, and then the green compacts were sintered at different temperatures under vacuum ($1 * 10^{-3}$ Pa). The sintering procedure is shown in Fig. 2. First, to completely remove the binder paraffin in the sample, the temperature was raised to 400°C at a ramping rate of 2°C/min and maintained for 2 h. Next, the green body was sintered at 1400, 1450 or 1500°C for 2 h at a ramping rate of 5°C/min. After sintering, the sample was naturally cooled to room temperature. Table II shows the composition and sintering temperature of the samples in this work.

### Characterizations

Prior to characterization, the sintered samples were ground with 600 to 2000 grit SiC sandpapers and polished to remove surface contamination. The phase compositions of the as-synthesized powders

**Table I. Composition of raw material mixtures for the preparation of 20 g 1 vol.%, 5 vol.%, 10 vol.% and 20 vol.% $MoSi_2$-$WSi_2$ composite powders**

| | Raw materials (g) | | | Products (g) | |
|---|---|---|---|---|---|
| **Sample** | **$MoS_2$** | **$WS_2$** | **Si** | **$MoSi_2$** | **$WSi_2$** |
| $MoSi_2$-1 vol.% $WSi_2$ | 21.06 | 0.32 | 14.81 | 19.70 | 0.30 |
| $MoSi_2$-5 vol.% $WSi_2$ | 19.82 | 1.53 | 14.48 | 18.54 | 1.46 |
| $MoSi_2$-10 vol.% $WSi_2$ | 18.32 | 2.98 | 14.11 | 17.15 | 2.85 |
| $MoSi_2$-20 vol.% $WSi_2$ | 15.55 | 5.69 | 13.40 | 14.55 | 5.45 |

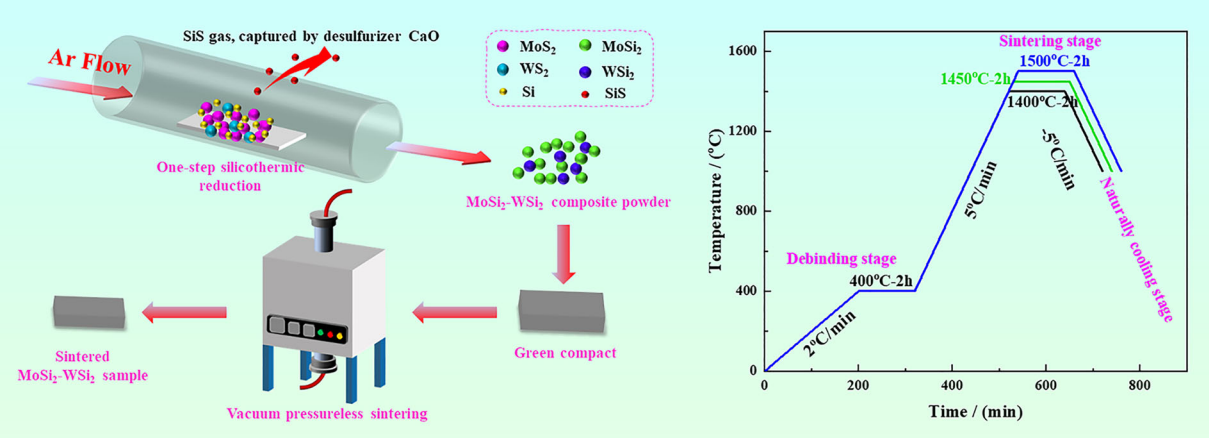


Fig. 1. Schematic illustration of the preparation and sintering schedule for the $MoSi_2$, $WSi_2$ and $MoSi_2$-$WSi_2$ composite powders.

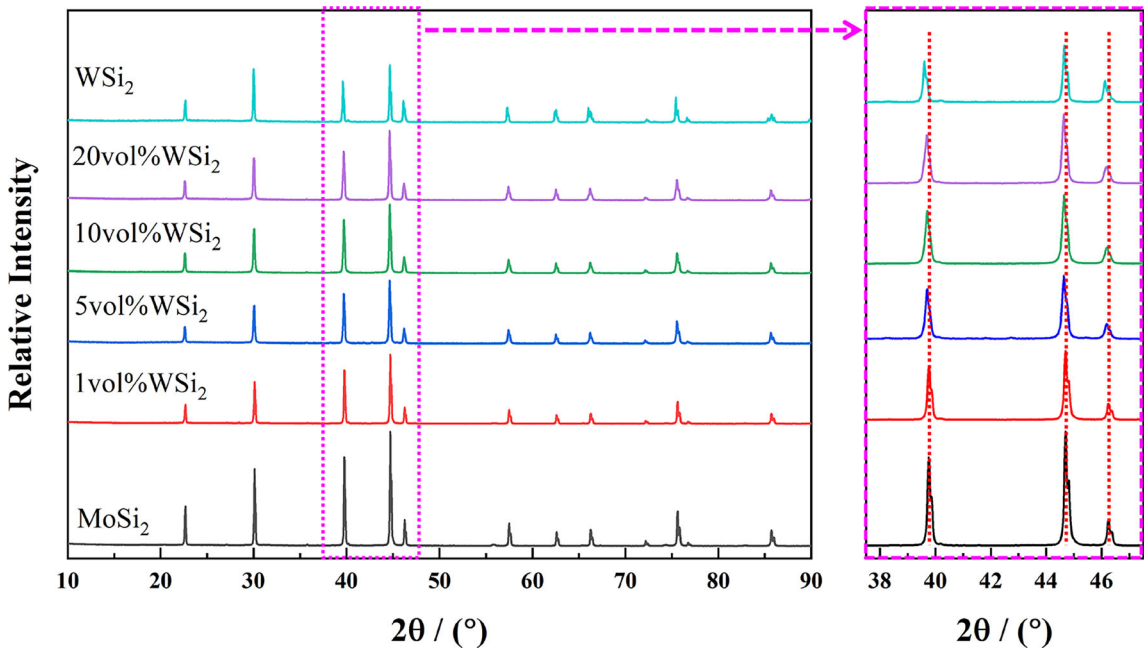


Fig. 2. XRD patterns of the powders with different compositions ($MoSi_2$, $MoSi_2$-1 vo l%$WSi_2$, $MoSi_2$-5 vol.% $WSi_2$, $MoSi_2$-10 vol.% $WSi_2$, $MoSi_2$-20 vo l%$WSi_2$ and $WSi_2$) prepared at 1100°C for 2 h.

and sintered samples were characterized by X-ray diffraction (XRD; TTR III, Rigaku Corporation, Japan; X-ray wavelength, 1.5418 Å [Cu-Kα], the step size and scan rate for the XRD experiment are 0.02° and 30 °/min, respectively.). Their morphologies, microstructures and element distributions were analyzed by field-emission scanning electron microscopy (FE-SEM; ZEISS SUPRA 55,

**Table II. Temperatures for powder preparation and sintering as well as corresponding relative density of the sintered samples**

| Number | Powder preparation | Sintering | Relative density (%) |
|---|---|---|---|
| 1 | $MoSi_2$-1100°C | 1400°C | 80.3 |
| 2 | $MoSi_2$-1100°C | 1450°C | 84.46 |
| 3 | $MoSi_2$-1100°C | 1500°C | 89.94 |
| 4 | $MoSi_2$-1000°C | 1500°C | 89.43 |
| 5 | $MoSi_2$-1200°C | 1500°C | 86.01 |
| 6 | $MoSi_2$-1 vol.% $WSi_2$-1100°C | 1500°C | 91.09 |
| 7 | $MoSi_2$-5 vol.% $WSi_2$-1100°C | 1500°C | 92.43 |
| 8 | $MoSi_2$-10 vol.% $WSi_2$-1100°C | 1500°C | 94.36 |
| 9 | $MoSi_2$-20 vol.% $WSi_2$-1100°C | 1500°C | 95.21 |
| 10 | $WSi_2$-1100°C | 1500°C | 85.22 |

Oberkochen, Germany) equipped with energy dispersive X-ray spectrometer (EDS). The preparation process of the powder sample for SEM observation is as follows: First, the obtained product was gently crushed and ground with an agate mortar and then sieved (200 mesh). Subsequently, about 0.05 g powder was dispersed on the conductive adhesive (adhered to the aluminum plate). Finally, a conductive gold film was coated on the surface of the powder for electron microscope observation.

The relative density of the sintered samples was estimated from lattice parameters based on XRD data. The theoretic density of the prepared $MoSi_2$-$WSi_2$ solid solution phase can be calculated by Eq. 2, where $m$, $V$ and $M$ are the mass, volume and relative molecular mass of the prepared $MoSi_2$-$WSi_2$ solid solution phase single cell; $a$ as well as $c$ are the lattice parameters; $N_A$ is the Avogadro constant ($6.02 \times 10^{23}$). By Eq. 1, the theoretic densities of $MoSi_2$-1 vo l%$WSi_2$, $MoSi_2$-5 vol.% $WSi_2$, $MoSi_2$-10 vol.% $WSi_2$, $MoSi_2$-20 vo l%$WSi_2$ composites are calculated to be 6.33, 6.46, 6.62 and 6.96 g/cm$^3$, respectively (see supplemental material Table S1). The Vickers hardness ($HV$) of the sintered samples was measured using a digital microhardness tester (THV-1MDX, Test-tech Ltd., China) under a load of 98 N for 15 s, and the $HV$ can be established by Eq. 3[27] where $F$, $S$, $\alpha$, $d$ and $P$ are the load (N), surface area of the indentation (mm$^2$), relative angle of the indenter (136°), average diagonal length of the indentation (mm) and load (kg), respectively. In addition, the fracture toughness ($K_{IC}$) value was estimated by Eq. 4.[6,28]

$$\rho = \frac{m}{V} = \frac{M/N_A}{a^2 c} \quad (2)$$

$$HV = 0.102 * \frac{F}{S} = 0.102 * \frac{2F\sin\frac{\alpha}{2}}{d^2} = 1.8544 * \frac{P}{d^2} \quad (3)$$

$$K_{IC} = \mathrm{A}\left(\frac{E}{H}\right)^{1/2} \frac{P}{c^{3/2}} \quad (4)$$

where A, $E$, $H$, $P$ and $c$ are the constant of 0.016, elastic modulus (440 GPa),[29] Vickers hardness (GPa), load (gf) and average of the four-surface radial crack length ($\mu$m), respectively. The flexural strength was measured at room temperature using a three-point bending strength analyzer (CDW, Changchun Chaoyang Test Instrument Ltd., China) with a span length of 12 mm (bend sample dimension was 3 mm * 4 mm * 14 mm).

## RESULTS AND DISCUSSION

### Powder Preparation Analysis

Our previous work showed that the temperatures required for synthesizing $MoSi_2$ or $WSi_2$ powders via silicothermic reduction of $MoS_2$ and $WS_2$ are about 1000°C and 1100°C, respectively.[24,25] Therefore, 1100°C was selected as the temperature for the synthesis of $MoSi_2$-$WSi_2$ composite powders. The XRD patterns of samples with different compositions ($MoSi_2$, $MoSi_2$-1 vo l%$WSi_2$, $MoSi_2$-5 vol.% $WSi_2$, $MoSi_2$-10 vol.% $WSi_2$, $MoSi_2$-20 vo l%$WSi_2$ and $WSi_2$) prepared at 1100°C for 2 h are shown in Fig. 2. Since $MoSi_2$ and $WSi_2$ have similar crystal structure, the Bragg peaks are quite close, making it hard to distinguish $MoSi_2$ and $WSi_2$. By magnifying the local XRD patterns, it can be clearly found that the diffraction peaks gradually deviate to a lower angle with the increase of $WSi_2$ content in the powder. In general, the shift of XRD diffraction peaks to lower angles implies an increase of the lattice constant, which is usually due to the doping of heteroatoms with a radius larger than that of the host atoms.[30] The atomic radius of Mo is 0.139 nm, while that of W is 0.141 nm, so the solid solution of $WSi_2$ in $MoSi_2$ will make the XRD diffraction peaks shift to a lower angle.

The microscopic morphologies of the samples with different compositions prepared at 1100°C for 2 h are shown in Fig. 3. Apparently, the prepared powder particles inherited the overall size and sheet-like morphology of $MoS_2$ or $WS_2$, and the synthesized powder particles consisted of a great

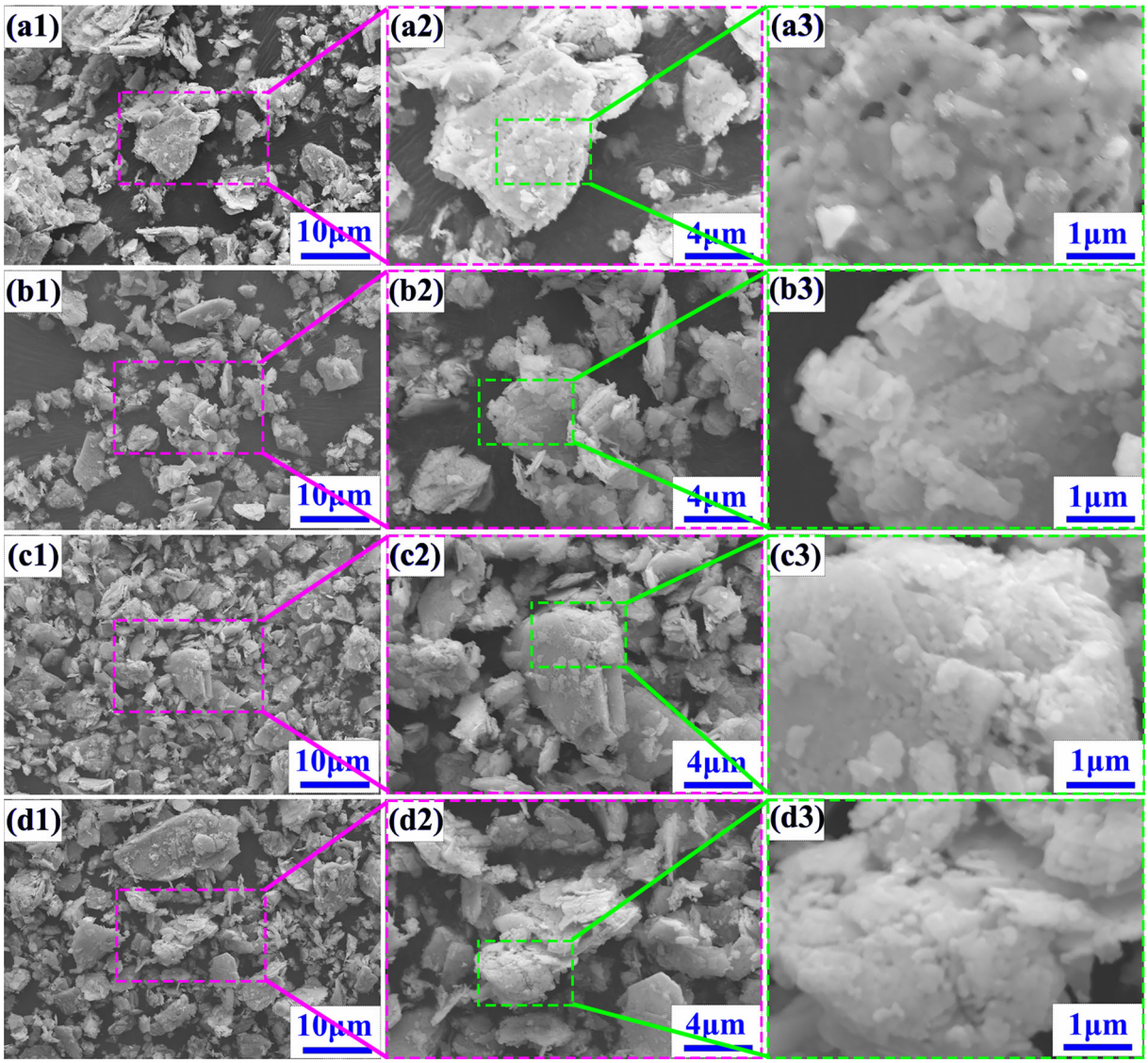


Fig. 3. FE-SEM images of the samples with different compositions prepared at 1100°C for 2 h: (a) $MoSi_2$-1 vo l%$WSi_2$, (b) $MoSi_2$-5 vol.% $WSi_2$, (c) $MoSi_2$-10 vol.% $WSi_2$ and (d) $MoSi_2$-20 vo l%$WSi_2$.

many of ultrafine grains. Additionally, the microscopic morphologies of the $MoSi_2$ powders acquired at 1000, 1100 and 1200°C as well as the $WSi_2$ powder synthesized at 1100°C can be found from our previous report.[24,25] The average grain sizes of the $MoSi_2$ particles synthesized at 1000°C, 1100°C and 1200°C after reacting for 2 h were about 100 nm, 300 nm and 1 $\mu$m, respectively.[24]

To verify whether $WSi_2$ is completely dissolved in $MoSi_2$, the elemental distribution of the as-prepared $MoSi_2$-20 vo l%$WSi_2$ composite powder was observed using FE-SEM equipped with EDS. As Fig. S2 shows (see supplemental material), the elements W, Mo and Si are uniformly distributed. However, on some small particles (marked with red or green circles), there are only W and Si but no Mo elemental distribution. Therefore, $WSi_2$ is not completely solid-dissolved in $MoSi_2$ because of the lower preparation temperature. Similarly, for the $MoSi_2$-$WSi_2$ composite powders prepared by MA, $WSi_2$ also cannot completely form a solid solution with $MoSi_2$.[20]

## Relative Density and Microstructure of Sintered Samples

### *Relative Density Analysis*

First, the effect of temperature on the sintering was studied using $MoSi_2$ powder prepared at 1100°C as raw material. The relative densities of the sintered $MoSi_2$ samples at 1400, 1450 and 1500°C for 2 h are shown in Table II. Obviously, as the sintering temperature increases from 1400°C to 1450°C and then to 1500°C, the relative density of the samples increases from 80.30% to 84.46% and then to 89.94%. Sintering temperature is an

important factor affecting sintering. In a certain temperature range, high temperature is beneficial to increase the atomic diffusion ability, promote the formation and growth of sintered necks, and improve the relative density of sintered samples.

The effect of particle sizes of prepared powders on the sintering was studied using the $MoSi_2$ powders obtained at 1000, 1100 and 1200°C as raw materials, and the green compacts were sintered at 1500°C for 2 h under vacuum. As Table II shows, the relative densities of the sintered samples are 89.43%, 89.94% and 86.01%, respectively. In general, finer powders have greater sintering activity.[5] However, the size of the particles also affects the relative density of green body. Specifically, density measurements showed that the relative densities of the green compacts of $MoSi_2$ powders obtained at 1000, 1100 and 1200°C were 45.06%, 49.22% and 49.53%, respectively. That is, during sintering, compacts with the powder obtained at 1000°C require greater shrinkage to achieve the same relative density than samples with the powders obtained at 1100°C or 1200°C. This results in powders prepared at 1000°C not showing a significant densification advantage over those prepared at 1100°C and 1200°C under the current sintering conditions.

The melting points of $MoSi_2$ and $WSi_2$ are 2030°C and 2160°C, respectively. As Table II shows, the relative density of the sintered $WSi_2$ sample is only 85.22%, which is lower than that of $MoSi_2$ (89.43%) under the same sintering conditions, indicating that $WSi_2$ is more difficult to densify than $MoSi_2$. Therefore, the densification degree of sintered $MoSi_2$-$WSi_2$ composite samples should decrease with the increase of $WSi_2$ volume fraction.[5] However, as the volume fraction of $WSi_2$ in $MoSi_2$-$WSi_2$ composite powder increases from 0% to 1%, 5%, 10% and then to 20%, the relative density of the sintered samples increases from 89.94% to 91.09%, 92.43%, 94.36% and 95.21% (Tables II and S1). This is contrary to the expected result; the reason for this anomaly will be explained in the next section.

### *Phase and Microstructure Analysis*

XRD patterns of the sintered samples with different compositions obtained at 1500°C are shown in Fig. 4. Similar to the XRD patterns of powders shown in Fig. 1, the diffraction peaks also gradually deviate to a lower angle with the increase of $WSi_2$ content in the sample.

The backscattered electron (BSE) image and corresponding element distribution maps of the sintered $MoSi_2$-10 vol.% $WSi_2$ sample are shown in Fig. 5. Clearly, Mo and W elements are uniformly distributed throughout the field of view, proving that $WSi_2$ is completely dissolved in $MoSi_2$ after sintering. In the BSE image, two distinct phases can be found, the gray matrix phase and white secondary phase. The EDS spectrum corresponding to the position A exhibits that only Mo, W and Si elements can be identified, while in the white secondary phase (corresponding to position B), Fe element can be found in addition to Mo, W and Si.

The BSE images of the sintered samples of $MoSi_2$, $MoSi_2$-1 vo l%$WSi_2$, $MoSi_2$-5 vo l%$WSi_2$ and $MoSi_2$-20 vo l%$WSi_2$ are shown in Fig. 6a, b, c, and d, respectively. Apparently, for the sintered $MoSi_2$ sample, only the gray matrix phase can be found. In addition, white secondary phases can be found in the sintered 1, 5 and 20 vol.% $MoSi_2$-$WSi_2$ composite samples, and its proportion increases with the increase of $WSi_2$ volume fraction. Therefore, the Fe element in the product should be introduced by the raw material $WS_2$.

The FE-SEM image and corresponding element distribution maps of $WS_2$ reagent are shown in Fig. 7. It can be found that the $WS_2$ reagent contains a small amount of Fe element, and the EDS spectrum shows that the amount of Fe in $WS_2$ reagent is about 0.42 wt.%. Furthermore, the Fe content in the $WS_2$ reagent and sintered samples was accurately assessed depending on Chinese national standard GB/T 6730.5-2022. The results show that the Fe contents in the $WS_2$ reagent and the sintered samples of $MoSi_2$-1 vo l%$WSi_2$, $MoSi_2$-5 vo l%$WSi_2$, $MoSi_2$-10 vo l%$WSi_2$ and $MoSi_2$-20 vo l%$WSi_2$. composites were 0.49 wt.%, 0.01 wt.%, 0.04 wt.%, 0.09 wt.% and 0.14 wt.%, respectively.

The melting point of Fe is 1535°C, which is lower than that of $MoSi_2$ and $WSi_2$, and Fe is reported to be an effective sintering aid for $TiB_2$ (with a melting point of 2980°C) and $B_4C$ (with a melting point of 2450°C) + $TiB_2$.[31,32] Therefore, herein, the presence of Fe also acts as a sintering aid for $MoSi_2$-$WSi_2$ composites, which explains why the relative density increases with the increase of $WSi_2$ volume fraction in the sintered samples.

## Mechanical Properties of Sintered Samples

Figure 8 and Table III show the room temperature mechanical properties of the sintered samples. The Vickers hardness, fracture toughness and flexural strength of the sintered $MoSi_2$ and $WSi_2$ samples are 8.02 GPa and 7.23 GPa, 2.33 MPa $m^{1/2}$ and 2.36 MPa $m^{1/2}$, as well as 211 MPa and 157 MPa, respectively. Many works have demonstrated that $WSi_2$ has higher hardness than $MoSi_2$,[33,34] and the inferior mechanical properties of the sintered $WSi_2$ sample in this work can be attributed to the lower densification degree (85.22%). The mechanical properties of the currently sintered $MoSi_2$ sample are much higher than those of the $MoSi_2$ sample obtained by vacuum pressureless sintering at 1550°C with micron-sized Si and Mo as raw materials.[36] This is because the $MoSi_2$ powder particles prepared in this work are composed of a many of ultrafine grains and have good sintering activity. However, the mechanical properties of the sintered $MoSi_2$ sample are lower

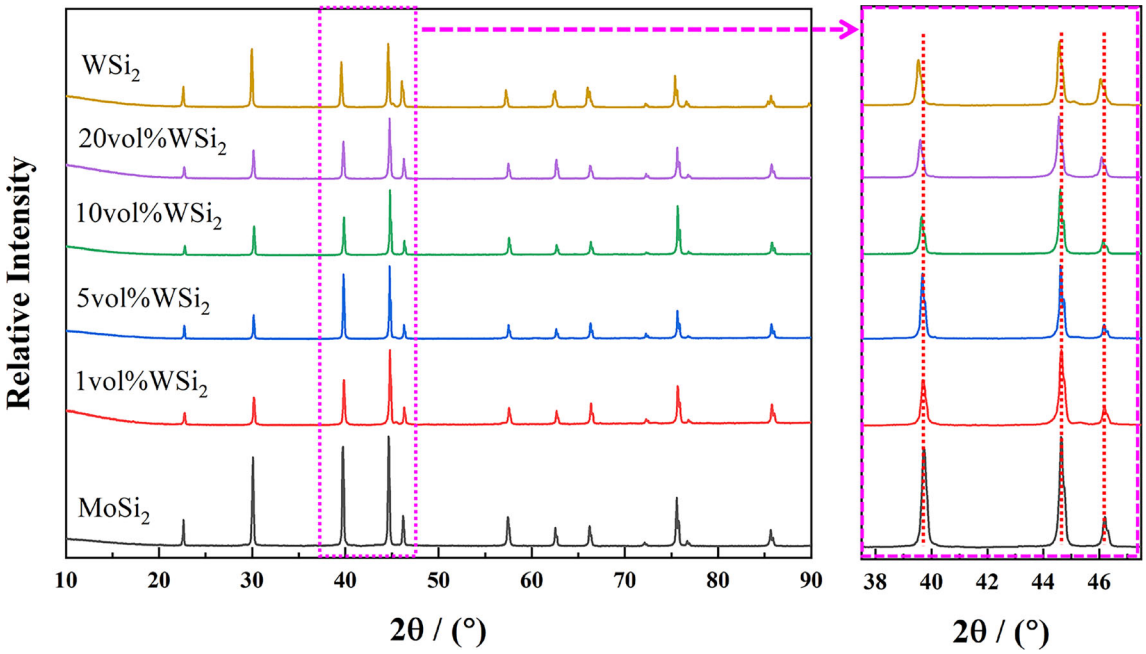


Fig. 4. XRD patterns of the sintered samples with different compositions ($MoSi_2$, $MoSi_2$-1 vol.% $WSi_2$, $MoSi_2$-5 vol.% $WSi_2$, $MoSi_2$-10 vol.% $WSi_2$, $MoSi_2$-20 vol.% $WSi_2$ and $WSi_2$) obtained at 1500°C.

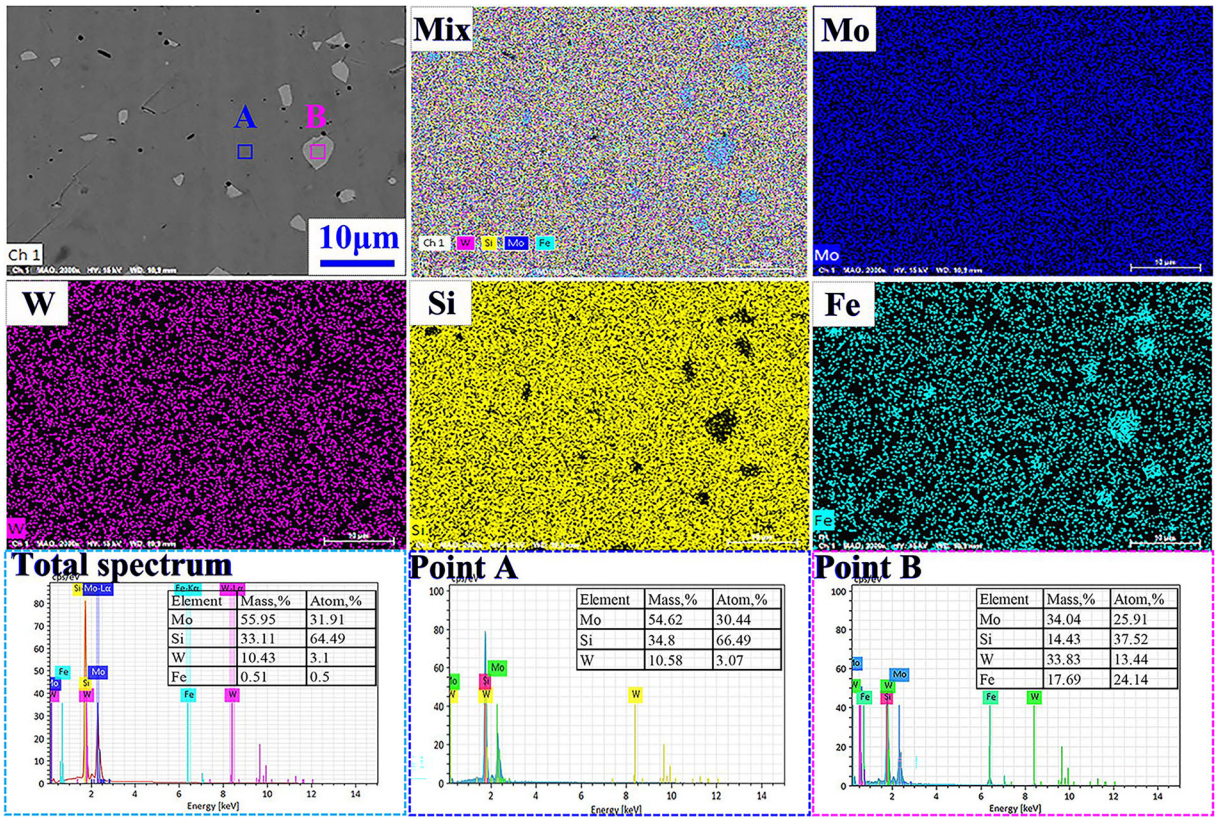


Fig. 5. BSE image and corresponding element distribution maps of the sintered sample with composition of $MoSi_2$-10 vol.% $WSi_2$.

than those of the $MoSi_2$ samples prepared by HP and SPS process.[5,6,37–40] Table III shows that even at a temperature of 1200°C, a sintered $MoSi_2$ sample with a relative density of 94.74% can be acquired by HP sintering, and the relative density increases with the increase of temperature. Likewise, the Vickers hardness and fracture toughness of the sintered $WSi_2$ sample in this work are lower

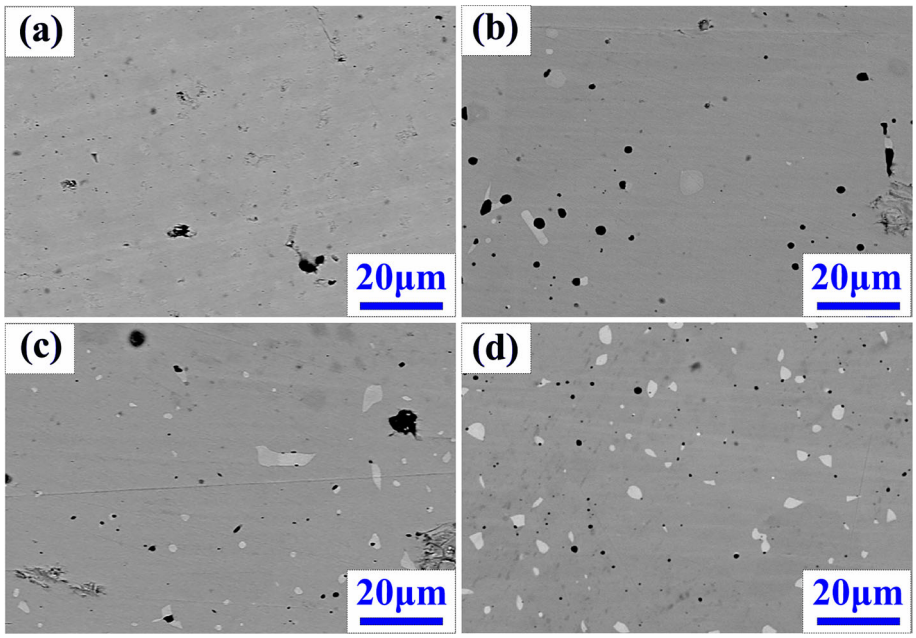


Fig. 6. BSE images of the sintered samples of (a) $MoSi_2$, (b) $MoSi_2$-1 vo l%$WSi_2$, (c) $MoSi_2$-5 vo l%$WSi_2$ and (d) $MoSi_2$-20 vo l%$WSi_2$.

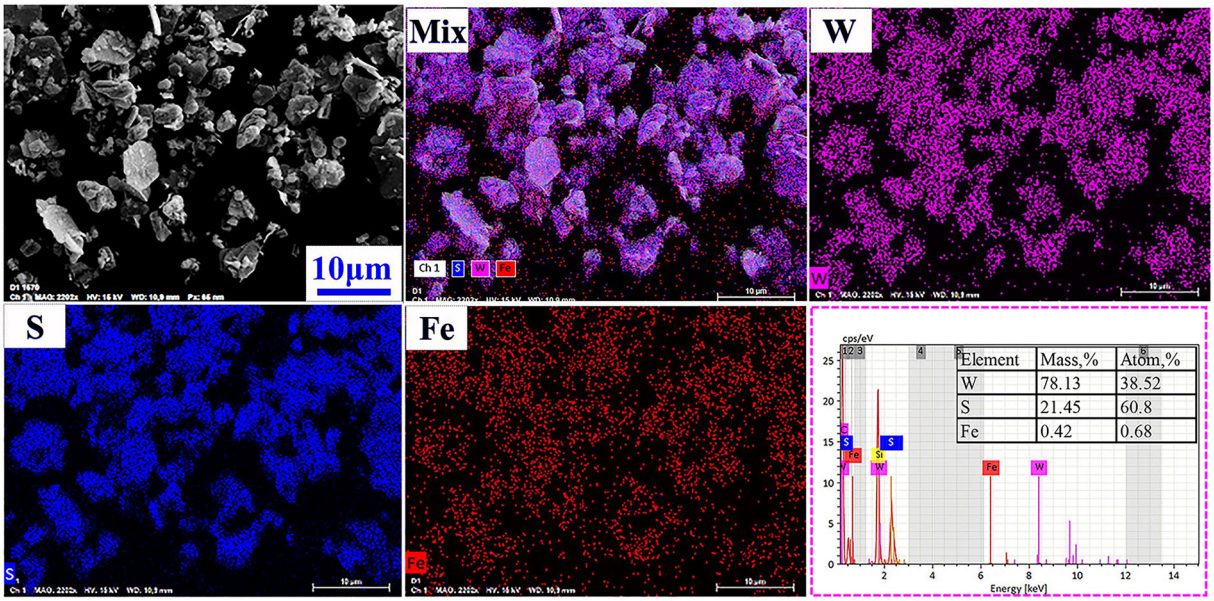


Fig. 7. FE-SEM image and corresponding element distribution maps of $WS_2$ reagent.

than those of the $WSi_2$ sample prepared by HP sintering.[41] Obviously, the relative density of the sintered samples is an important factor affecting its mechanical properties.

The Vickers hardness of the sintered $MoSi_2$-$WSi_2$ composite samples increases with the increase of $WSi_2$ volume fraction, with the highest Vickers hardness of 10.72 GPa achieved by sample $MoSi_2$-20 vol.% $WSi_2$. Chen et al.[5] have proved that the Vickers hardness of $MoSi_2$-$WSi_2$ sintered samples increases with the increase of $WSi_2$ volume fraction (Table III). In addition, the increase in relative density is also favorable to improve the Vickers hardness. Figure 8 also exhibits that with the increase of the $WSi_2$ volume fraction, the fracture toughness of the sintered $MoSi_2$-$WSi_2$ composite samples first increases and then decreases. The sintered $MoSi_2$-10 vol.% $WSi_2$ sample has the highest fracture toughness of 7.28 MPa $m^{1/2}$, which is 3.12 times that of pure $MoSi_2$ in this work. Furthermore, this value is close to that of the $MoSi_2$-10 vol.% $WSi_2$ sample obtained by vacuum pressureless sintering at 1550°C (6.69–7.32 MPa $m^{1/2}$)[20] and higher than the $MoSi_2$-10 vol.% $WSi_2$ sample (5.89 MPa $m^{1/2}$) prepared using the SPS sintering process.[5]

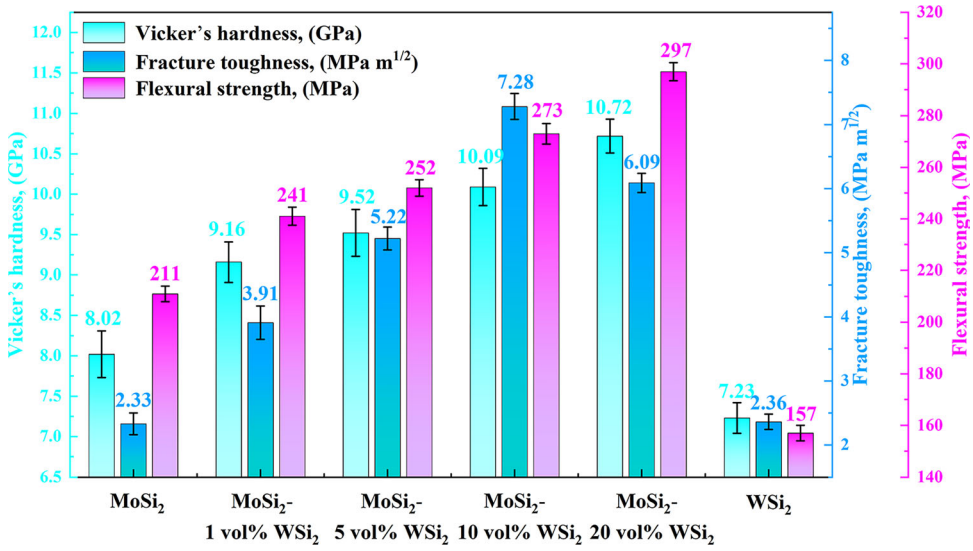


Fig. 8. Mechanical properties of sintered samples.

Similar to the Vickers hardness, the flexural strength of the $MoSi_2$-$WSi_2$ composite sample increases with increasing $WSi_2$ volume fraction, which can be attributed to the increase in the relative density of the samples. The $MoSi_2$-20 vol.% $WSi_2$ composite sample has the highest flexural strength of 297 MPa, which is 40.76% greater than that of the sintered $MoSi_2$ sample prepared under the same conditions. The bending fracture morphologies of the sintered samples with different compositions are shown in Fig. 9. Figure 9a1, a2, f1, and f2 shows that there are obvious pores in the sintered $MoSi_2$ and $WSi_2$ samples, suggesting the low densification degree. In particular, the relative density of the sintered $WSi_2$ sample is only 85.22%, which is lower than that of $MoSi_2$ (89.43%) under the same sintering conditions, indicating that $WSi_2$ is difficult to densify compared to the other five samples. Additionally, Figure 9a1, a2 to e1, and e2 shows that the dominant fracture mode of $MoSi_2$ is transgranular, while the fracture of $MoSi_2$-$WSi_2$ composite samples is more tortuous and intergranular than that of the $MoSi_2$ sample, bringing about a significant improvement of fracture toughness.[5]

According to the dislocation theory, grain boundaries are obstacles for dislocation movement. Under the action of external force, to produce shear deformation in the adjacent grains, the grain boundary must generate a large enough stress concentration. Since grain refinement means more grain boundaries, if the grain boundary structure remains unchanged, a greater external force must be applied to generate dislocation accumulation, thereby strengthening the material.[42] In addition, based on the Hall-Petch relationship (Eq. 5, where $\sigma_0$ and $k_1$ are constants, and $d$ is the grain diameter), the fracture strength $\sigma_f$ is inversely proportional to the square root of the grain diameter $d$, that is, the smaller the grain, the higher the fracture strength will be.[43] In this work, the grain size distributions of the sintered samples were determined by software Image J based on Fig. 9, and the results are shown in Fig. S3 (see supplemental material). As Fig. S3 shows, the average grain sizes of synthesized $MoSi_2$, $MoSi_2$-1 vol.% $WSi_2$, $MoSi_2$-5 vol.% $WSi_2$, $MoSi_2$-10 vol.% $WSi_2$, $MoSi_2$-20 vol.% $WSi_2$ and $WSi_2$ are 11.9, 8.3, 9.4, 7.5, 5.4 and 1.5 $\mu$m, respectively. Clearly, the grains are gradually refined with the increase of $WSi_2$ fraction volume. Consequently, the improved mechanical properties of the $MoSi_2$-$WSi_2$ sintered samples can be attributed to the grain refinement.

$$\sigma_f = \sigma_0 + k_1 d^{-\frac{1}{2}} \tag{5}$$

For brittle ceramic materials, the relationship between fracture strength $\sigma_f$ and porosity can be expressed by Eq. 6, where $\sigma_0$ is the theoretically fracture strength of the sample without pores; $P$ is the volume fraction of porosity, and $b$ is a material-dependent constant between 4 and 6.[44] The relative density of the sintered $MoSi_2$-$WSi_2$ composite samples increases with the addition of $WSi_2$, that is, the porosity of the samples decreases gradually. Therefore, there will be an enhancement of mechanical properties of the sintered samples of $MoSi_2$-$WSi_2$.

$$\sigma_f = \sigma_0 \exp(-bP) \tag{6}$$

In conclusion, ultrafine $MoSi_2$-$WSi_2$ composite powders were obtained by silicothermic reduction of $MoS_2$-$WS_2$ mixtures, and sintered $MoSi_2$-$WSi_2$ composite samples with competitive mechanical properties were acquired via vacuum pressureless sintering. Compared with the sintered $MoSi_2$ sample, the improved mechanical properties of the sintered $MoSi_2$-$WSi_2$ composite samples can be

**Table III. Room temperature mechanical properties of sintered $MoSi_2$, $WSi_2$ and $MoSi_2$-based samples (* represents this work)**

| Composition | Sintering condition | Relative density (%) | Vickers hardness (GPa) | Fracture toughness (MPa $m^{1/2}$) | Flexure strength (MPa) |
|---|---|---|---|---|---|
| $MoSi_2$ * | Vacuum pressureless, 1500°C | 89.43 | 8.02 | 2.33 | 211 |
| $WSi_2$ * | Vacuum pressureless, 1500°C | 85.22 | 7.23 | 2.36 | 157 |
| $MoSi_2$-1 vol.% $WSi_2$* | Vacuum pressureless, 1500°C | 91.09 | 9.16 | 3.91 | 241 |
| $MoSi_2$-5 vol.% $WSi_2$* | Vacuum pressureless, 1500°C | 92.43 | 9.52 | 5.22 | 252 |
| $MoSi_2$-10 vol.% $WSi_2$* | Vacuum pressureless, 1500°C | 94.36 | 10.09 | 7.28 | 273 |
| $MoSi_2$-20 vol.% $WSi_2$* | Vacuum pressureless, 1500°C | 95.21 | 10.72 | 6.09 | 297 |
| $MoSi_2$[36] | Vacuum pressureless, 1550°C | 78.7 | 0.871 | - | 97.75 |
| $MoSi_2$[35] | HP, 30 MPa, 1700°C | > 96 | 10 | 2.58 | - |
| $MoSi_2$[37] | HP, 41.4 MPa, 1640°C | 95.3 | - | 2.5–3 | 140 ~ 160 |
| $MoSi_2$[6] | HP, 5.5 GPa, 1300°C | 99.7 | 15 | 10.7 | - |
| $MoSi_2$[38] | HP, 30 MPa, 1650°C | 98.4 | 8.7 | 3.1 | 253 |
| $MoSi_2$[39] | SPS, 40 MPa, 1300°C | 99.3 | 9.3 | 2.8 | 249 |
| $MoSi_2$[40] | SPS, 30 MPa, 1500°C | 97.29 | 9.5 | 4.1 | 255 |
| $MoSi_2$[5] | SPS, 40 MPa, 1200°C | 94.74 | 9.69 | 2.63 | - |
| $WSi_2$[40] | HP , 60 MPa, 1300°C | 96.5 | 13.43 | 3.3 | - |
| $MoSi_2$-5 vol.% $WSi_2$[5] | SPS, 40 MPa, 1200°C | 96.63 | 11.55 | 6.02 | - |
| $MoSi_2$-10 vol.% $WSi_2$[5] | SPS, 40 MPa, 1200°C | 96.27 | 13.91 | 5.89 | - |
| $MoSi_2$-15 vol.% $WSi_2$[5] | SPS, 40 MPa, 1200°C | 95.87 | 14.55 | 5.07 | - |
| $MoSi_2$-20 vol.% $WSi_2$[5] | SPS, 40 MPa, 1200°C | 95.74 | 16.47 | 4.79 | - |
| $MoSi_2$-20 vol.% $WSi_2$[20] | Vacuum pressureless, 1550°C | 87.27 | 9.72 | 6.69 | 210 |
| $MoSi_2$-20 vol.% $WSi_2$[20] | Vacuum pressureless, 1550°C | 91.13 | 10.56 | 6.69 | 242 |
| $MoSi_2$-20 vol.% $WSi_2$[20] | Vacuum pressureless, 1550°C | 96.49 | 10.78 | 7.32 | 327 |

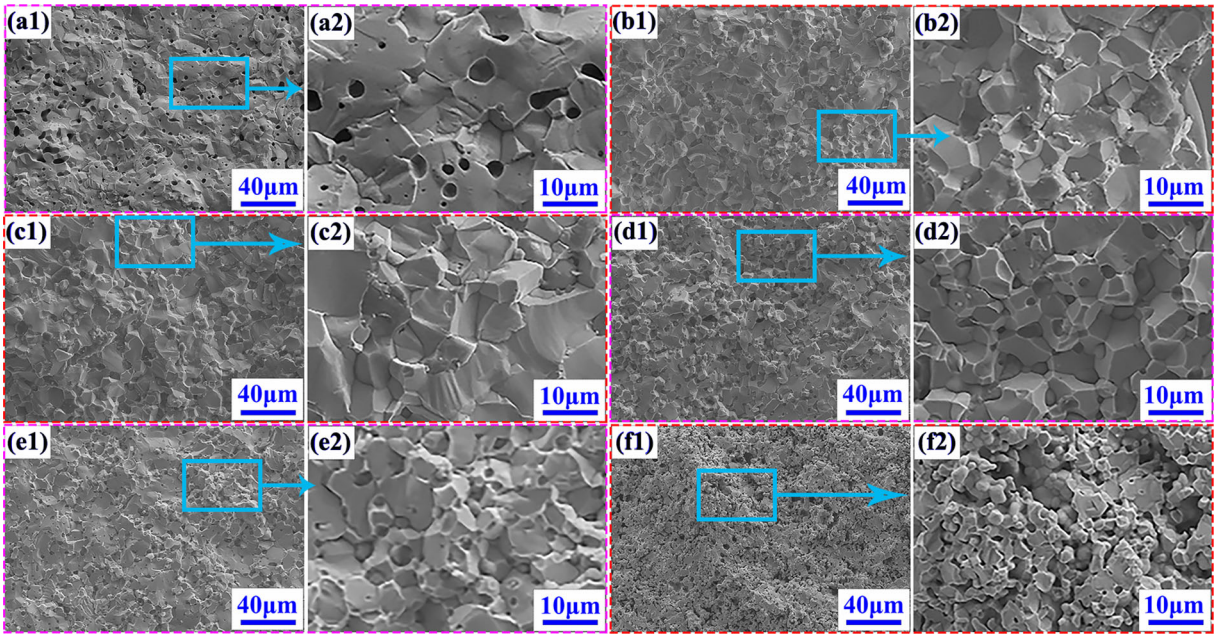


Fig. 9. Bending fracture morphologies of the sintered samples with different compositions: (a1 and a2) $MoSi_2$, (b1 and b2) $MoSi_2$-1 vol.% $WSi_2$, (c1 and c2) $MoSi_2$-5 vol.% $WSi_2$, (d1 and d2) $MoSi_2$-10 vol.% $WSi_2$, (e1 and e2) $MoSi_2$-20 vol.% $WSi_2$ and (f1 and f2) $WSi_2$.

ascribed to the solid solution strength of $WSi_2$, grain refinement and the increase in the relative density of the samples caused by the introduction of Fe element.

## CONCLUSION

This work proposed a new route to synthesize ultrafine $MoSi_2$-$WSi_2$ composite powders with different volume fractions of $WSi_2$. Subsequently, the

vacuum pressureless sintering behavior of the prepared powders was studied. Additionally, the microstructure and mechanical properties of the sintered samples were further explored. The following conclusions can be drawn:

1. $MoSi_2$-$WSi_2$ composite powders with different $WSi_2$ volume fractions (1 vol.%, 5 vol.%, 10 vol.% and 20 vol.%) were successful synthesized via silicothermic reduction of $MoS_2$-$WS_2$ mixtures. FE-SEM images showed that the prepared $MoSi_2$-$WSi_2$ composite powder particles inherited the overall size and sheet-like morphology of $MoS_2$ or $WS_2$, and are composed of many ultrafine grains.
2. The elemental distribution maps of the prepared $MoSi_2$-$WSi_2$ composite powders showed that $WSi_2$ was not completely dissolved in $MoSi_2$. After vacuum pressureless sintering at 1500°C, $WSi_2$ was completely dissolved in $MoSi_2$.
3. The Fe element introduced by $WS_2$ reagent acted as sintering aid and improved the relative density of the sintered $MoSi_2$-$WSi_2$ composite samples.
4. The addition of $WSi_2$ to $MoSi_2$ matrix can significantly improve its mechanical properties, attributed to the solid solution strength of $WSi_2$, grain refinement and increase of relative density of the samples caused by the introduction of Fe element. When the volume fraction of $WSi_2$ was between 1% and 20%, after sintering at 1500°C for 2 h, the $MoSi_2$-20 vol.% $WSi_2$ composite sample had the highest densification degree, hardness and flexural strength of 95.21%, 10.72 GPa and 297 MPa, respectively. The $MoSi_2$-10 vol.% $WSi_2$ composite sample had a relative density of 94.36% and a maximum fracture toughness value of 7.28 MPa $m^{1/2}$.

## CONFLICT OF INTEREST

There are no conflicts to declare.

## SUPPLEMENTARY INFORMATION

The online version contains supplementary material available at https://doi.org/10.1007/s11837-023-05973-6.

## ACKNOWLEDGEMENTS

This work was financially supported by the State Key Laboratory of Advanced Metallurgy, University of Science and Technology Beijing, China.

## REFERENCES

1. X. Chen, and C. Liang, *Catal Sci Technol.* 1, 1 https://doi.org/10.1039/C9CY00533A (2019).
2. H.Q. Chang, H.Y. Wang, G.H. Zhang, and K.C. Chou, *Ceram Int.* https://doi.org/10.1016/j.ceramint.2021.11.329 (2022).
3. E. Tekoğlu, Y. Yürektürk, D. Ağaoğulları, D. Ovalı, S. Mertdinc, and M.L. Öveçoğlu, *Adv. Powder. Technol.* https://doi.org/10.1016/j.apt.2019.08.010 (2019).
4. Z. Yao, J. Stiglich, and T.S. Sudarshan, *J. Mater. Eng. Perform.* https://doi.org/10.1361/105994999770346837 (1999).
5. F. Chen, J. Xu, Y. Liu, and L. Cai, *Ceram Int.* 1, 1 https://doi.org/10.1016/j.ceramint.2016.04.023 (2016).
6. H. Liang, F. Peng, H. Chen, L. Tan, Q. Zhang, C. Fan, S. Guan, X. Ni, A. Liang, X. Yan, and Q. Hu, *Mater. Sci. Eng. A.* https://doi.org/10.1016/j.msea.2017.11.016 (2018).
7. T.J. Trentler, R.S. Iyer, S.M.L. Sastry, and W.E. Buhro, *Chem. Mater.* https://doi.org/10.1021/cm010267c (2001).
8. S. Zamani, H.R. Bakhsheshi-Rad, M.R.A. Kadir, and M.R.M. Shafiee, *J. Alloys Compd.* 1, 1 https://doi.org/10.1016/j.jallcom.2012.06.072 (2012).
9. Y.L. Jeng, and E.J. Lavernia, *J. Mater. Sci.* https://doi.org/10.1007/BF00356804 (1994).
10. D. Yi, and C. Li, *Mat. Sci. Eng. A.* https://doi.org/10.1016/S0921-5093(98)01053-3 (1999).
11. J.J. Petrovic, A.K. Bhattacharya, R.E. Honnell, T.E. Mitchell, R.K. Wade, and K.J. McClellan, *Mater. Sci. Eng. A.* https://doi.org/10.1016/0921-5093(92)90332-U (1992).
12. J.F. Huang, B. Wang, H.J. Li, M. Liu, L.Y. Cao, and C.Y. Yao, *Corros. Sci.* https://doi.org/10.1016/j.corsci.2010.11.024 (2011).
13. T. Minasyan, L. Liu, Y. Holovenko, S. Aydinyan, and I. Hussainova, *Ceram Int.* https://doi.org/10.1016/j.ceramint.2019.02.035 (2019).
14. Z.G. Liu, W. Li, J.L. Fan, Y.Z. Lv, Z.W. Wang, and X.J. Zhao, *Ceram Int.* https://doi.org/10.1016/j.ceramint.2021.12.310 (2022).
15. J. Arreguín-Zavala, S. Turenne, A. Martel, and A. Benaissa, *Mater. Charact.* https://doi.org/10.1016/j.matchar.2012.03.014 (2012).
16. H. Hu, X. Wu, R. Wang, W.G. Li, and Q. Liu, *Intermetallics.* https://doi.org/10.1016/j.intermet.2015.07.008 (2015).
17. A.A. Sharif, A. Misra, J.J. Petrovic, and T.E. Mitchell, *Intermetallics*. https://doi.org/10.1016/S0966-9795(01)00084-X (2001).
18. J. Subrahmanyam, and R.M. Rao, *Mater. Sci. Eng. A.* https://doi.org/10.1016/0921-5093(94)90904-0 (1994).
19. J.J. Petrovic and R.E. Honnell, Hoboken, NJ, USA: John Wiley & Sons, Inc 1990, pp.734–744. https://doi.org/10.1002/9780470313008.ch17.
20. J.G. Xu, Y.C. Wang, B.C. Weng, and F. Chen, *Mater. Trans.* https://doi.org/10.2320/matertrans.M2014370 (2015).
21. J.G. Xu, Y. Leng, H.Q. Li, and H.A. Zhang, *Int. J. Refract. Met H.* https://doi.org/10.1016/j.ijrmhm.2008.03.005 (2009).
22. S.R. Srinivasan, and R.B. Schwarz, Elastic moduli of $MoSi_2$-based materials. *J. Mater. Res.* 7, 1610–1613 https://doi.org/10.1557/JMR.1992.1610 (1992).
23. H.Q. Chang, G.H. Zhang, and K.C. Chou, *J. Am. Ceram Soc.* https://doi.org/10.1111/jace.17994 (2021).
24. H.Q. Chang, and G.H. Zhang, *Ceram Int.* https://doi.org/10.1016/j.ceramint.2022.07.121 (2022).
25. H.Q. Chang, and G.H. Zhang, *Powder .Technol.* https://doi.org/10.1016/j.powtec.2022.118102 (2022).
26. H. Chu, T.M. Lillo, B. Merkle, D.W. Bailey, M. Harrison, Ballistic Properties of Pressureless Sintered SiC/$TiB_2$ Composites. In Advances in Ceramic Armor: A Collection of Papers Presented at the 29th International Conference on Advanced Ceramics and Composites, (John Wiley & Sons, Inc, Hoboken, 2005), pp. 279–286.
27. G.R. Anstis, P. Chantikul, B.R. Lawn, and D.B. Marshall, *J. Am. Ceram Soc.* https://doi.org/10.1111/j.1151-2916.1981.tb10320.x (1981).
28. A.G. Evans, and E.A. Charles, *J. Am. Ceram Soc*. https://doi.org/10.1111/j.1151-2916.1976.tb10991.x (1976).
29. H. Liang, F. Peng, C. Fan, Q. Zhang, J. Liu, and S.X. Guan, *Chin. Phys. B.* https://doi.org/10.1088/1674-1056/26/5/053101 (2017).

30. B. Zhang, F. Yang, X. Liu, N. Wu, S. Che, and Y. Li, *Appl. Catal. B-Environ.* https://doi.org/10.1016/j.apcatb.2021.120494 (2021).
31. S.H. Kang, D.J. Kim, E.S. Kang, and S.S. Beak, *J. Am. Ceram Soc.* https://doi.org/10.1111/j.1151-2916.2001.tb00763.x (2001).
32. H. Latifi, A. Moradkhani, H. Baharvandi, and J. Martikainen, *Mater. Design.* https://doi.org/10.1016/j.matdes.2014.05.039 (2014).
33. M. Nakamura, S. Matsumoto, and T. Hirano, *J. Mater. Sci.* 25, 3309–3313 https://doi.org/10.1007/BF00587691 (1990).
34. Y. Pan, C. Jing, and Y.P. Wu, *Vacuum*. https://doi.org/10.1016/j.vacuum.2019.06.035 (2019).
35. J.J. Petrovic, and R.E. Honnell, *J. Mater. Sci.* https://doi.org/10.1007/BF00581107 (1990).
36. F. Chen, J. Xu, and Z. Hou, *Ceram Int.* https://doi.org/10.1016/j.ceramint.2011.11.046 (2012).
37. F.D. Gac, and J.J. Petrovic, *J. Am. Ceram Soc.* https://doi.org/10.1111/j.1151-2916.1985.tb10182.x (1985).
38. K. Peng, M.Z. Yi, L.P. Ran, and Y.C. Ge, *J. Am. Ceram Soc.* https://doi.org/10.1111/j.1551-2916.2007.01971.x (2007).
39. X.X. Han, Y.L. Wang, X. Xiong, H. Li, Z.K. Chen, and W. Sun, *Trans. Nonferr. Metal. Soc.* https://doi.org/10.1016/S1003-6326(18)64730-2 (2018).
40. H. Shimizu, M. Yoshinaka, K. Hirota, and O. Yamaguchi, *Mater. Res. Bull.* https://doi.org/10.1016/S0025-5408(02)00852-8 (2002).
41. D.Y. Oh, H.C. Kim, J.K. Yoon, I.Y. Ko, and I.J. Shon, *Met. Mater. Int.* https://doi.org/10.1007/BF03027547 (2006).
42. H. Van Swygenhoven, *Science*. https://doi.org/10.1126/science.107104 (2002).
43. N. Hansen, *Scripta mater.* https://doi.org/10.1016/j.scriptamat.2004.06.002 (2004).
44. X. Fan, E.D. Case, F. Ren, and M.J. Baumann, *J Mec Behav Biomed.* https://doi.org/10.1016/j.jmbbm.2011.12.014 (2012).